Monthly Notices of the ROYAL ASTRONOMICAL SOCIETY

MNRAS **543,** 1224–1238 (2025) https://doi.org/10.1093/mnras/staf1537
Advance Access publication 2025 September 13

The halo mass dependence of physical and observable properties in the circumgalactic medium at $z = 0$

Andrew W. S. Cook [1]★ Freeke van de Voort [1] Rüdiger Pakmor [2] and Robert J. J. Grand [3]

[1]*Cardiff Hub for Astrophysics Research and Technology, School of Physics and Astronomy, Cardiff University, Queens Building, The Parade, Cardiff CF24 3AA, UK*
[2]*Max-Planck-Institut für Astrophysik, Karl-Schwarzschild-Str 1, D-85748 Garching, Germany*
[3]*Astrophysics Research Institute, Liverpool John Moores University, 146 Brownlow Hill, Liverpool L3 5RF, UK*

Accepted 2025 September 9. Received 2025 September 9; in original form 2024 September 7

ABSTRACT

We study the dependence of the physical and observable properties of the circumgalactic medium on its halo mass in 25 high-resolution cosmological 'zoom-in' simulations from the Auriga suite. We focus on the current epoch ($z = 0$) and on halo masses of 10^{10} M$_\odot \leq M_{200c} \leq 10^{12}$ M$_\odot$ and stellar masses of 10^7 M$_\odot \leq M_\star \leq 10^{11}$ M$_\odot$. The mass resolution of our simulations is 5.4×10^3 M$_\odot$. This work analyses the temperature, density, metallicity, and radial velocity of these haloes and the column density of H I, Mg II, Si II, C IV, and O VI. We find median temperature and metallicity increase with halo mass as expected. We find a larger scatter in temperature at higher halo masses, suggesting that the multiphase nature of the CGM is halo-mass-dependent. Our H I column densities show good agreement with observations at all radii. Mg II and Si II match observations between $0.1\,R_{200c}$ and $0.3\,R_{200c}$, but decrease steeply with radius. O VI column densities are underpredicted by our simulations for stellar masses in the range $10^{9.5}$ M$_\odot \leq M_\star < 10^{10.2}$ M$_\odot$ at large radii with reasonable agreement at 10^{11} M$_\odot$. C IV column densities agree with observational detections above a halo mass of $10^{9.5}$ M$_\odot$. We find that O VI (H I) traces the highest (lowest) temperatures, and the lowest (highest) density and metallicity. O VI (C IV) is photoionized (collisionally ionized) at low (high) halo masses with a transition to higher temperatures at 10^{11} M$_\odot$. Our results demonstrate similarities and discrepancies between simulations of Milky Way-mass haloes and observations. They also show further observational constraints are needed in less massive haloes.

Key words: MHD – methods: numerical – galaxies: dwarf – galaxies: evolution – galaxies: haloes – cosmology: theory.

1 INTRODUCTION

The circumgalactic medium (CGM) is the gaseous component of dark-matter-dominated haloes. It surrounds galaxies and contains gas accreted from the intergalactic medium (IGM) and gas ejected from the interstellar medium (ISM). The CGM plays a major role in the evolution of galaxies, acting as a reservoir for baryonic matter that can accrete on to the ISM and provide fuel for star formation (Tumlinson, Peeples & Werk 2017).

The CGM features various temperature phases, which range from 10^4 K (or lower if we account for molecular outflows) up to approximately the virial temperature (or potentially hotter in outflows). These gas phases are probed observationally primarily through absorption line spectroscopy as it is sensitive down to column densities of $N \approx 10^{12}$ cm^{-2}, making it an effective method of characterizing the low-density CGM. Absorption line spectroscopy traces ions with different ionization potentials to detect various gas temperatures, and thus the multiphase nature, of the CGM (Lehner et al. 2013; Anand, Nelson & Kauffmann 2021; Mathur et al. 2021).

Quantifying the physical nature of the CGM is important to further our understanding of its role in galaxy evolution. We know from simulations and analytical arguments that the hydrodynamical properties of the CGM depend not only on feedback from the galaxy, but also on the halo mass (e.g. Frenk et al. 1988; Wang & Abel 2008; van de Voort & Schaye 2012). Haloes with masses similar to the Milky Way (10^{12} M$_\odot$) are typically hot (T $\approx 10^6$ K) and metal-rich with higher accretion rates on to the galaxy than lower mass haloes (Kereš et al. 2005; Tumlinson et al. 2011).

Feedback from galaxies, driven by stellar winds, supernovae (SNe), and active galactic nuclei (AGNs), ejects matter into the CGM, which enriches the environment with metals (Muratov et al. 2015; Johnson et al. 2017; Sanchez et al. 2019). The strong feedback from star-forming galaxies means that only 20–25 per cent of all metals produced are retained in their ISM (Peeples et al. 2014). Material ejected by these feedback processes either flows out of the CGM into the IGM and beyond, remains in the CGM, or re-accretes on to the galaxy. This re-accretion is likely important at late times as it can dominate the accretion rate (Oppenheimer et al. 2010; Hafen et al. 2020; Wright et al. 2021) and could be important for maintaining star formation in the galaxy.

Outflows from feedback also change the ionization states of metals by heating the gas. Low ionization states such as H I, Si II, and Mg II trace cool gas (T $= 10^4$ K) in the CGM, with C IV tracing warmer gas of $10^{4.5-5}$ K. Higher ionization states such as O VI potentially trace warm–hot temperatures, if in collisional ionization equilibrium (CIE), of $10^{5.5}$ K (Gnat & Sternberg 2007; Wiersma, Schaye &

★ E-mail: andrewwscook96@gmail.com

Smith 2009; Strawn, Roca-Fàbrega & Primack 2023) but these may trace cooler temperatures if in photoionization equilibrium (PIE) (McQuinn & Werk 2018).

The ionization states of gas in the CGM can be probed in simulations too, utilizing radiative transfer or non-equilibrium chemistry models (e.g. AREPO-RT and RAMSES-RTZ; Kannan et al. 2019; Katz 2022) or post-processing tools such as TRIDENT (Hummels, Smith & Silvia 2017), which uses CLOUDY (Ferland et al. 2017) for its ionization tables. Mock observables have been compared to observations before with varying results. Machado et al. (2018) show over predictions in the O VI and Si III column densities when compared to observations. Studies also show good agreement for synthetic absorption lines and equivalent widths, and covering fractions from SIMBA consistent with observations (Appleby et al. 2021). The aim of these comparisons is to assist in constraining our models, thus leading to better predictions in future simulation work.

In this work, we analyse cosmological zoom-in simulations to determine the dependence of the temperature, density, metallicity, and radial velocity on halo mass for haloes with a mass range of 10^{10} $M_\odot \leq M_{200c} \leq 10^{12}$ $M_\odot$. The aim of this work is to better understand the CGM in a cosmological context by quantifying the scatter in the physical properties as a function of halo mass and galactocentric radius. Furthermore, we compare the column densities for H I, Mg II, Si II, C IV, and O VI, in our simulations with observational surveys including COS-Halos (Tumlinson et al. 2013; Werk et al. 2016), COS-Dwarfs (Bordoloi et al. 2014), the CIViL* survey (Garza et al. 2025), the CGM^2 survey (Tchernyshyov et al. 2022), the Cosmic Ultraviolet Baryon Survey (CUBS) (Mishra et al. 2024), as well as other observational studies (Johnson, Chen & Mulchaey 2015; Zheng et al. 2024) to better understand how our model compares to the existing observations and find discrepancies that we can use to inform future models.

This paper is structured as follows. We briefly outline the Auriga simulations, including how these haloes are selected in Section 2. We will then discuss the physical properties of the CGM in our simulated haloes in Section 3. We compare the results of our column densities to those from observations in Section 4. Finally, we conclude and discuss our results in Section 5.

2 THE AURIGA SUITE OF COSMOLOGICAL SIMULATIONS

This work studies the CGM of 25 high-resolution simulations from the Auriga project – a suite of magnetohydrodynamical (MHD) cosmological zoom-in simulations (Grand et al. 2017, 2024). The simulations we analyse have a baryonic mass resolution of $\sim 5.4 \times 10^3$ $M_\odot$ (also referred to as 'level 3') and a dark matter resolution of $\sim 4 \times 10^4$ $M_\odot$. We additionally perform a resolution test comparing the level 3 simulations used in this paper with haloes at eight times higher (level 2) and lower (level 4) resolutions. This is discussed in Section 5.2.

The initial conditions of Auriga are based on the dark-matter-only simulations from the EAGLE project (Schaye et al. 2015), with a co-moving box size of 100 Mpc. Haloes are identified using a friends-of-friends (FoF) algorithm with a standard linking length (Davis et al. 1985). Haloes are randomly selected from the 25 per cent most isolated haloes within the targeted mass range (see Grand et al. 2017). The mass selection criterion for Milky Way-mass haloes is $0.5 < M_{200c}/10^{12}$ $M_\odot < 2$ and less massive haloes were selected within $0.5 < M_{200c}/10^{11}$ $M_\odot < 5$ and $0.5 < M_{200c}/10^{10}$ $M_\odot < 5$. The high-resolution zoom-in region extends to $\sim 5 R_{200c}$ of each halo. Auriga adopts cosmological parameters $\Omega_m = 0.307$, $\Omega_b = 0.048$, and $\Omega_\Lambda = 0.693$ with $H_0 = 100h$ km s^{-1} Mpc^{-1}, where $h = 0.6777$ from Planck Collaboration XVI (2014).

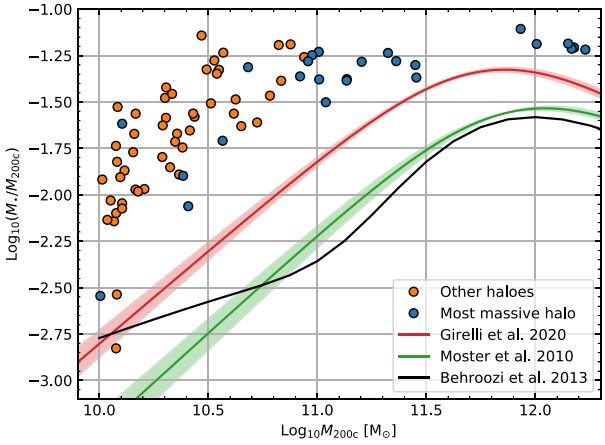

Figure 1. Stellar mass to halo mass (SM–HM) ratio against halo mass. The blue data points show the SM–HM ratio for the most massive halo from each simulation. We compare them to three models from Moster et al. (2010), Behroozi et al. (2013), and Girelli et al. (2020) shown as green, black, and red curves, respectively. The scatter of Girelli et al. (2020) and Moster et al. (2010) is shown as the shaded regions. Compared to these models, our simulations overpredict the SM–HM ratio but generally follow the same trend.

The simulations were run from $z = 127$ to $z = 0$ using the arbitrary Lagrangian–Eulerian moving-mesh code AREPO (Springel 2010), which includes MHD for gas and collisionless dynamics (for dark matter, stars, and black holes). AREPO uses an unstructured Voronoi mesh with idealized MHD solved by a finite-volume second-order Runge–Kutta integration scheme (Pakmor et al. 2016). The inclusion of MHD to this suite of simulations has been shown to affect the properties and structure of the CGM at least for Milky Way-mass systems (van de Voort et al. 2019).

The Auriga galaxy formation model is described fully in Grand et al. (2017) and summarized here. The ISM subgrid model in these simulations is described in Springel & Hernquist (2003) as a two-phase medium of dense cold gas clouds surrounded by hotter ambient gas. The gas in the ISM is assumed to be star-forming once the density exceeds a threshold density of $n_{\rm H}^* = 0.11$ cm^{-3}. Gas that is above this density threshold is treated as multiphase and its temperature is governed by an equation of state that is calculated as part of a subgrid model. These simulations additionally include primordial and metal line-cooling (Vogelsberger et al. 2013) as well as an ultraviolet background with self-shielding (Faucher-Giguère et al. 2009; Rahmati et al. 2013). The metal yields used include asymptotic giant branch stars (Karakas 2010), Type Ia SN (Thielemann et al. 2003; Travaglio et al. 2004), and core-collapse SN (Portinari, Chiosi & Bressan 1998).

Auriga incorporates feedback from SN, stellar winds, and AGNs. Stellar feedback is implemented through gas cells that are temporarily converted into collisionless wind particles, ejected from star-forming gas, until they reach 5 per cent of $n_{\rm H}^*$ where they recouple and deposit mass, momentum, thermal energy, and metals. The minimum temperature in our simulations is set to 10^4 K because cooling below this temperature is inefficient.

AGN feedback is modelled as a two-mode process: one that heats the gas locally around the black hole and the other that gently heats bubbles of gas at randomly placed locations up to 80 per cent of the virial radius. Black holes are seeded in the simulations with a mass of

Table 1. Properties of the most massive haloes in each of our simulations ordered by halo mass from top to bottom in ascending order. (*a*) simulation reference name, (*b*) halo mass, (*c*) virial temperature, (*d*) virial radius of halo, (*e*) stellar mass, (*f*) star formation rate, (*g*) the mass of the CGM (measured within the virial radius and excluding ISM gas), (*h*) the mass of the ISM. The baryonic mass resolution of these haloes is 5.4×10^3 $M_\odot$.

Halo ID[a]	$\mathrm{Log}_{10} M^b_{200c}$ ($M_\odot$)	T^c_{vir} (K)	R^d_{200c} (kpc)	SFR[e] ($M_\odot$ yr^{-1})	$\mathrm{Log}_{10} M^f_\star$ ($M_\odot$)	$\mathrm{Log}_{10} M^g_{\mathrm{CGM}}$ ($M_\odot$)	$\mathrm{Log}_{10} M^h_{\mathrm{ISM}}$ ($M_\odot$)
			M_{200c}= 10^{10}–10^{11} $M_\odot$ haloes				
halo10_0	10.00	4.35	45.58	0.00	7.46	8.78	7.33
halo10_8	10.10	4.46	49.22	0.05	8.48	9.06	7.99
halo10_6	10.38	4.61	61.00	0.10	8.48	9.51	8.31
halo10_11	10.40	4.65	62.11	0.08	8.34	9.40	8.36
halo10_9	10.56	4.78	70.10	0.16	8.85	9.63	8.67
halo10_2	10.68	4.84	76.67	0.46	9.36	9.68	9.02
			M_{200c}= $\sim 10^{11}$–$10^{11.5}$ $M_\odot$ haloes				
halo11_10	10.92	4.88	92.07	0.47	9.55	9.91	9.11
halo11_11	10.95	4.98	94.72	0.89	9.67	9.93	9.30
halo11_6	10.97	4.94	96.06	0.52	9.72	9.95	9.18
halo11_0	11.00	4.89	98.36	0.79	9.77	9.73	9.11
halo11_9	11.00	4.89	98.47	0.62	9.63	9.99	9.16
halo11_8	11.03	5.06	100.82	0.46	9.53	10.11	9.17
halo11_2	11.13	5.11	108.48	0.78	9.74	10.18	9.36
halo11_7	11.20	5.07	114.38	1.41	9.92	10.13	9.53
halo11_1	11.32	5.14	125.47	2.06	10.08	10.21	9.69
halo11_3	11.36	5.21	129.18	1.15	10.08	10.32	9.39
halo11_4	11.45	5.33	138.67	1.43	10.08	10.42	9.64
halo11_5	11.45	5.35	138.17	0.60	10.14	10.42	9.29
			$M_{200c} \gtrsim 10^{12}$ $M_\odot$ haloes				
halo12_L8	11.93	5.57	200.20	5.71	10.82	10.68	10.08
halo12_6	12.00	5.58	211.83	2.71	10.81	10.66	9.89
halo12_21	12.15	5.71	236.69	10.27	10.96	10.90	10.25
halo12_23	12.17	5.71	241.50	4.60	10.97	10.79	10.12
halo12_24	12.17	5.76	239.57	7.67	10.95	10.84	10.08
halo12_16	12.18	5.81	241.53	4.20	10.96	10.96	10.11
halo12_27	12.23	5.70	251.40	4.20	11.01	10.84	10.04

10^5 h^{-1} $M_\odot$ when the FoF halo group has a mass $M_{\mathrm{FOF}} = 5 \times 10^{10}$ h^{-1} $M_\odot$. Ionizing radiation is also included in the AGN feedback model in the form of X-rays.

Fig. 1 shows the ratio of stellar mass to halo mass as a function of halo mass. This includes the 25 most massive haloes and 52 additional haloes within the zoom-in region of each simulation. We find our simulations overestimate the stellar mass based on abundance matching from Moster et al. (2010), Girelli et al. (2020), and Behroozi, Wechsler & Conroy (2013). The larger scatter seen in this figure of our low-mass haloes has also been found in other simulation suites with an explicit ISM model (Agertz et al. 2020; Gutcke et al. 2021; Sales, Wetzel & Fattahi 2022). If we take this figure at face value, our simulated dwarf galaxies have produced $\sim$10 times as much stellar mass as predicted through abundance matching and thus also 10 times as many metals. Although uncertainties in abundance matching are large for low-mass haloes, this also has implications for the distribution of metals in the CGM. This has been previously investigated in Grand et al. (2024) and Pakmor et al. (2016), which show similar over predictions in low-mass haloes.

We focus on gas within the virial radius (R_{200c}) of the halo, defined as the radius within which the density within it is approximately 200 times the critical density of the Universe. We exclude the ISM (or star-forming gas, i.e. all of the gas on the equation of state) to more appropriately measure the properties of the inner CGM. This is accomplished by removing the gas cells with a positive star formation rate. We study haloes within a halo mass range of 1×10^{10} $M_\odot \leq M_{200c} \lesssim 2 \times 10^{12}$ $M_\odot$, corresponding to a stellar mass range of $10^{7.5}$ $M_\odot \leq M_\star \leq 10^{11}$ $M_\odot$. Table 1 lists further information on the key properties of the most massive haloes in each of the 25 zoom-in simulations. The following is a brief overview of the simulations and a description of the post-processing method to obtain metal ion column densities.

We calculate the column density of H I, Mg II, Si II, C IV, and O VI in our simulations. We chose these ions because they are the most commonly observed ions through absorption line spectroscopy (Fox et al. 2005; Ranjan et al. 2022) and trace different temperature phases of the gas. The mass fraction of H I is calculated on-the-fly, whereas the mass fraction of the metal ions are calculated in post-processing. We use tables generated with CLOUDY (Ferland et al. 2017) by Hummels et al. (2017) and the radiation field from Faucher-Giguère et al. (2009) to compute the mass fraction of the ions. We can then use this ion fraction and the metal-specific mass fraction to calculate the column density along any sight-line in our simulations. We treat any pixel in a projection of the halo as a single line-of-sight measurement.

3 DEPENDENCE OF PHYSICAL PROPERTIES IN THE CGM ON HALO MASS

In this section, we use our cosmological simulations to quantify the temperature, density, metallicity, and radial velocity as a function of

halo mass and radius to obtain a broad understanding of the physical nature of the CGM in our simulations.

3.1 Physical nature of the CGM

Fig. 2 shows projections with a projection depth of $R_{200c}/8$ at $z = 0$ of the volume-weighted density and mass-weighted temperature, metallicity, and radial velocity for five haloes rotated such that the central galaxy is edge-on. The halo mass lies in the range $10^{10}-10^{12}$ $M_\odot$, increasing in mass intervals of 0.5 dex from top to bottom. The circles indicate the virial radius of each halo: 45, 70, 98, 139, and 212 kpc, from top to bottom.

For more massive haloes, the CGM is hotter, more enriched with metals, and has higher radial velocities, both inflowing (negative values) and outflowing (positive values). In our most massive halo (bottom row) bipolar outflows can be seen along the minor axis, which have high metallicity and radial velocities but show no significant temperature differences along this axis. High values along the minor axis are seen in radial velocity and metallicity but are lower along the major axis. The temperature and density typically decrease with radius with minor differences outside of the central $0.25R_{200c}$.

In contrast, our lowest mass haloes (top row) exhibit low scatter in their temperature, density, metallicity, and radial velocity. High values of each property are found in the centre of the halo. Because the radial velocity is low and the gas is mostly inflowing, metals cannot reach significant distances into the CGM, resulting in a deficit in metals in the outer CGM. Similarly the temperature of the CGM does not change significantly outside of the central $0.25R_{200c}$. Temperatures reach $\sim 10^{4.5}$ K at most and do not fluctuate much at fixed radii.

Fig. 3 shows the density, temperature, metallicity, and radial velocity as a function of halo mass for 77 haloes within the zoom-in region of our 25 simulations. We calculate the median and 16$^{\rm th}$ and 84$^{\rm th}$ percentile scatter for the gas within $0.3R_{200c}-1.0R_{200c}$ to exclude the dense cool gas in the centre. The blue circles show mass-weighted values and the orange squares show volume-weighted values. For clarity, the scatter is only shown for mass-weighted temperature, metallicity, and radial velocity and for the volume-weighted density. We additionally include the virial temperature from Mo, van den Bosch & White (2010) in the temperature panel shown by the black straight line:

$$T_{\rm vir} = \frac{1}{2}\frac{\mu m_{\rm p}}{k_{\rm b}}\frac{M_{200c}}{R_{200c}}, \quad (1)$$

where $T_{\rm vir}$ is the virial temperature, μ is the mean molecular weight, $m_{\rm p}$ is the mass of a hydrogen atom, and $k_{\rm b}$ is the Boltzmann constant. As expected, we find that the median temperature is higher in more massive haloes, increasing from $\sim 10^{4.0}$ K in our lowest mass haloes ($M_{200c} = 10^{10}$ $M_\odot$) up to temperatures of $\sim 10^6$ K at high masses ($M_{200c} = 10^{12}$ $M_\odot$). Furthermore, the scatter is wider at these high masses, with a range of $\sim$0.5 dex in low-mass haloes, increasing to $\sim$1.5 dex in high-mass haloes. This increase indicates that the CGM is more multiphase in more massive haloes. The 16$^{\rm th}$ percentile of most of our haloes above $M_{200c} > 10^{11.75}$ $M_\odot$ haloes are at temperatures above 10^4 K. Cool gas is still present just not in large quantities.

We additionally calculated the temperature probability density functions measured outside $0.3R_{200c}$, which is not shown. The haloes with mass $M_{200c} > 10^{11}$ $M_\odot$ exhibit a bimodal distribution of temperatures. The range of temperatures in $M_{200c} < 10^{11}$ $M_\odot$ haloes is $T = 10^4-10^5$ K and extends to $T = 10^4$–10^6 K for more massive haloes. All haloes show a strong halo-to-halo variation in the mass distribution of cool gas. Gas at temperatures close to the virial temperature is dominant by mass for R > 0.25 in most haloes.

The volume-weighted gas density shows no clear dependence on the halo mass. The scatter fluctuates by < 0.1 dex from halo to halo, but shows no clear trend with halo mass for either mass- or volume-weighted quantities. The scatter seen here is primarily caused by the decreasing trend in the average density from $0.3R_{200c}$ to R_{200c} (see Fig. 4).

The median metallicity has no clear dependence on halo mass for $M_{200c} < 10^{11}$ $M_\odot$ (low-mass haloes), with more metal-rich gas present in more massive haloes; median values cover a range from $\sim 10^{-5}$ to 10^{-1} in low-mass haloes to near solar values ($\sim 10^0$) in more massive haloes ($M_{200c} \geq 10^{11}$ $M_\odot$). The scatter is small in more massive haloes, decreasing from $\sim$4 ($\leq 10^{-5} - 10^{-0.5}$) dex to $\sim$1 dex ($10^{-1} - 10^0$) over our sample of haloes. We find that the most massive haloes in the zoom-in region, which were selected to be the most isolated, exhibit low metallicities. It is therefore possible that additional haloes located within the zoom-in region have gained metals from nearby systems. The AGN feedback present in Milky Way-mass galaxies and high star formation rates produce stronger outflows, therefore contributing to more metal enrichment in the outer CGM of more massive haloes.

The median radial velocity is about $-40 - 40$ km s^{-1} across the halo mass range. Inflows dominate slightly over outflows, but shows no clear dependence on halo mass. The scatter in radial velocity is more skewed towards inflows in less massive haloes ($M_{200c} < 10^{11.5}$ $M_\odot$), while more massive haloes show more balanced inflows and outflows.

The relationship between volume- and mass-weighted quantities changes for different properties. The volume- and mass-weighted values of temperature and radial velocity are similar. The volume-weighted metallicity is typically lower than the mass-weighted metallicity in low-mass haloes ($M_{200c} < 10^{11}$ $M_\odot$) though the difference is smaller in more massive haloes indicating metals are clumped in higher density gas.

3.2 Radial profiles

Fig. 4 shows the radial dependence of the temperature, density, metallicity, and radial velocity, for both inflowing (solid line) and outflowing (dashed line) gas, for the same five haloes as shown in Fig. 2. The solid curves show the median properties and the shaded region the 16$^{\rm th}$ and 84$^{\rm th}$ percentile scatter. The solid black line in the temperature profiles indicates the virial temperature. The haloes shown range in halo mass from 10^{10} to10^{12} $M_\odot$, increasing from left to right in steps of 0.5 dex. Properties are mass-weighted except density, which is volume-weighted.

The median temperature remains fairly constant at 10^4 K in the inner CGM (typically between $0.1R_{200c}$ and $0.25R_{200c}$ with some variation between haloes). This region is dominated by a non-star-forming extended gaseous disc. As matter accretes on to the CGM, the temperature has been shown to increase to values near the virial temperature (de Voort & Schaye 2012). As this gas gets closer to the centre, the gas reaches higher densities, and it is able to cool and join the central disc (Stern et al. 2019). The scatter in temperature of the gas in the outer CGM is larger in more massive haloes, indicating that the gas in the outer CGM ($R > 0.25R_{200c}$) is more multiphase compared to less massive haloes.

The highest densities (10^{-2}cm^{-3}) are found close to the centre of the halo, at around $0.15R_{200c}$, decreasing down to 10^{-5}cm^{-3} at the virial radius. The scatter is almost negligible in our 10^{10} $M_\odot$ haloes with very low scatter outside of $0.25R_{200c}$. The scatter above this

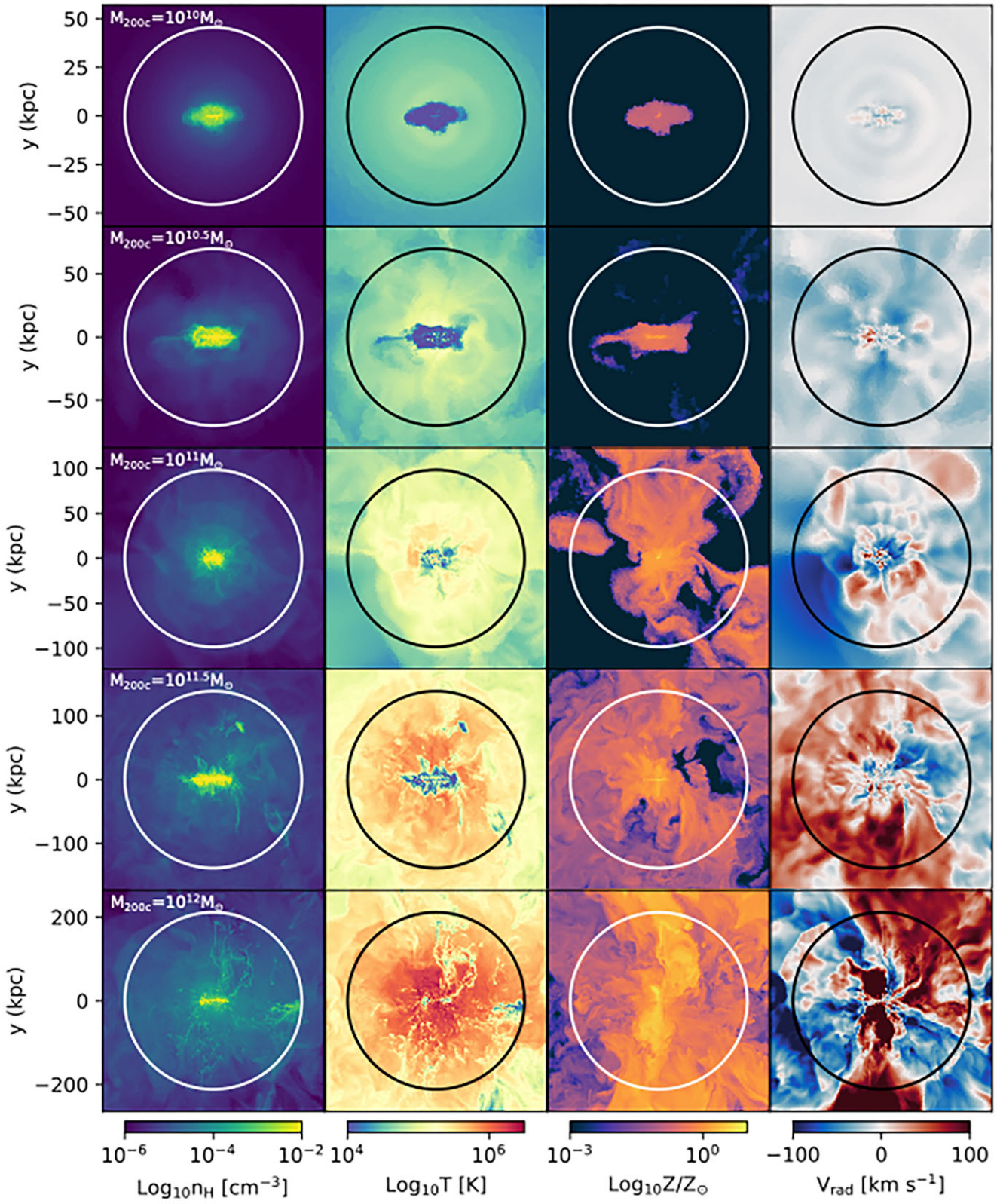

Figure 2. $2.5R_{200c} \times 2.5R_{200c}$ thin projections of five haloes, rotated such that the stellar disc is edge-on. Columns show, from left to right, the volume-weighted hydrogen number density and mass-weighted temperature, metallicity, and radial velocity with a projection depth of $R_{200c}/8$. The halo mass increases from top to bottom from $10^{10}-10^{12}$ $M_\odot$ in steps of 0.5 dex. The haloes in this Figure can be found in Table 1 as halo10_0, halo10_9, halo11_0, halo11_4, and halo12_6. The circle in each panel indicates the virial radius of each halo. When compared to high-mass haloes, low-mass haloes ($M_{200c} < 10^{11}$ $M_\odot$) contain gas with significantly lower temperatures and metallicities. Additionally, these haloes lack significant structure, whereas more massive haloes include cool dense filaments. The metallicity of the low-mass haloes is the highest in the centre but is still several orders of magnitude lower than the solar values of high-mass haloes. These low-mass haloes exhibit a sharp and steep drop off in metallicity outside of the centre. Metallicity outside of the centre of low-mass haloes drops below the lower bound set on our colour bar. The radial velocities are also significantly lower reaching values no higher than $\sim \pm 30$ km s^{-1}.

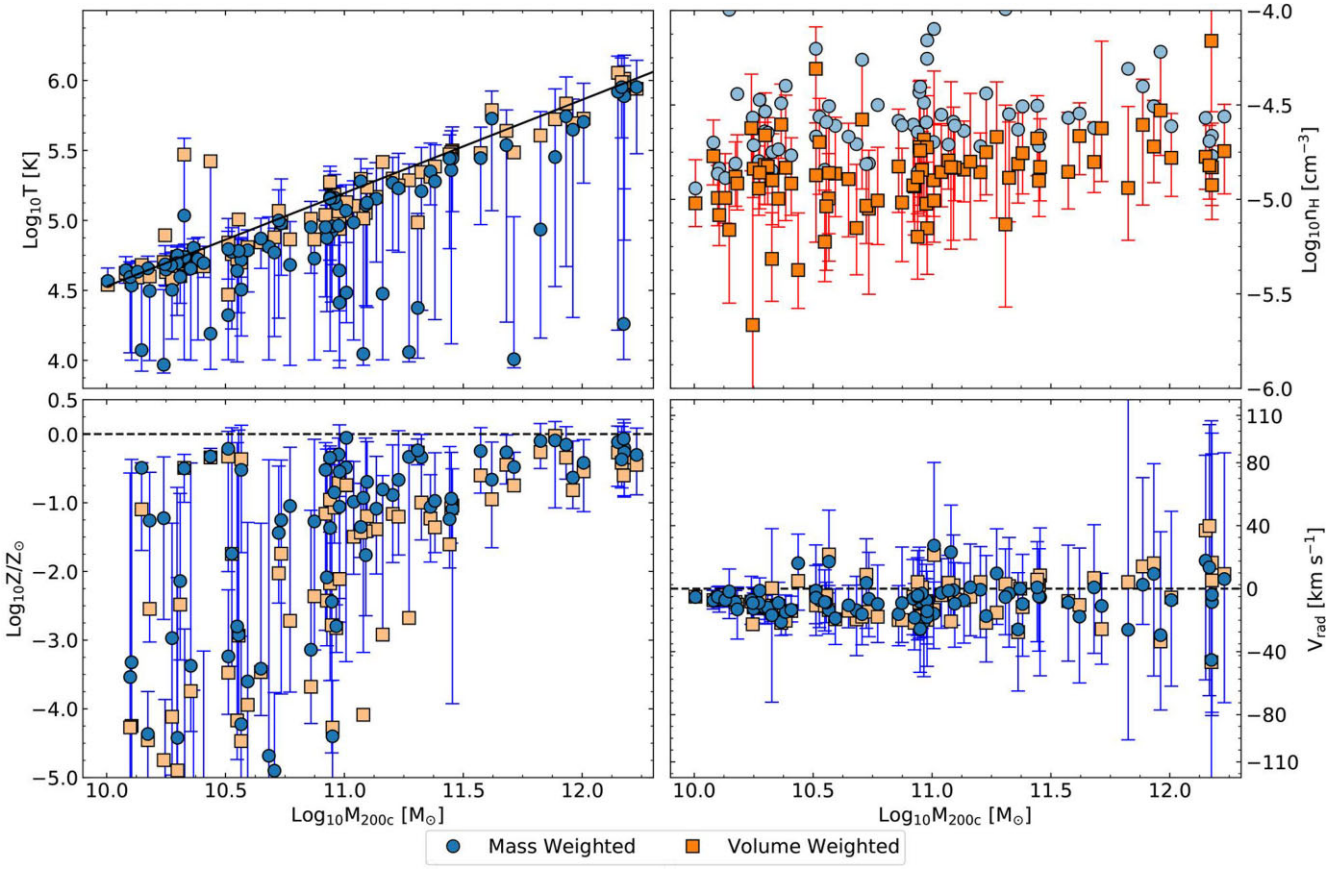

Figure 3. Median CGM temperature (top, left), hydrogen number density (top, right), metallicity (bottom, left), and radial velocity (bottom, right) for 77 haloes within the zoom-in region of our simulations as a function of halo mass with scatter bars showing the 16$^{\rm th}$ and 84$^{\rm th}$ percentiles. The scatter is only shown for mass-weighted (blue circles) temperature, metallicity, and radial velocity and for the volume-weighted (orange squares) density. We additionally include the virial temperature from Mo et al. (2010) in the temperature panel indicated by the solid black line. The properties are measured in the range $0.3 \leq R/R_{200c} \leq 1.0$ to remove the central galaxy and its extended H I-dominated disc. The temperature and metallicity vary strongly for our haloes, both in their median values and their scatter. There is no clear dependence on halo mass for the density. The scatter in radial velocity is wider in more massive haloes. However, the median radial velocity shows no clear trend with halo mass and is in most cases dominated by inflows.

halo mass is generally consistent for all other haloes. We see a radial dependence in the median profile but no change in scatter or halo mass dependence on gas density when volume-weighted. We separately calculated the mass-weighted density, which showed the same median trend as volume-weighted density. The density remains high at $\sim 10^{-1}$cm^{-2} out to larger radii than volume-weighted, typically out to $0.25R_{200c}$, before a sharp drop in density. Additionally, mass-weighted density shows somewhat higher scatter in more massive haloes.

The highest metallicity is seen in the centre of our haloes in the inner $\sim 0.25R_{200c}$. For our low-mass dwarfs, $M_{200c} < 10^{11}$ M$_\odot$, the metallicity decreases sharply because the outflows do not reach larger distances. The central metallicity is 1 dex lower in the 10^{10} M$_\odot$ halo compared to the 10^{11} M$_\odot$ halo. For more massive haloes ($M_{200c} \geq 10^{11}$ M$_\odot$) the median metallicity following a decreasing profile, with the scatter increasing with radius.

We see higher inflow and outflow velocities for more massive haloes. Both inflows and outflows follow similar trends within $0.25R_{200c}$ for all haloes. Haloes with $M_{200c} < 10^{11.5}$ M$_\odot$ have lower radial velocities in outflowing gas compared to inflowing gas outside of $0.25R_{200c}$, and are thus dominated by inflowing gas out to the virial radius. This is likely the result of weak stellar feedback because the wind velocity implemented in the Auriga galaxy formation model is equal to 3.46 times the one-dimensional dark matter velocity dispersion (Grand et al. 2017). More massive haloes exhibit faster outflows than low-mass haloes and similarly high inflows. Haloes with $M_{200c} \geq 10^{11.5}$ M$_\odot$ exhibit inflowing and outflowing gas increasing to a maximum radial velocity at roughly the same radius as the maximum temperature. At this point, the gas is in rotation leading to less inflowing and outflowing velocities closer to the centre of the halo.

4 COLUMN DENSITY OF THE CGM

It is important to understand how our simulations match or differ from observations. This will assist in understanding the validity of our models and how best we can improve them in future simulations.

We compare the column density (N_x where x is H I, Mg II, Si II, C IV, and O VI) of H I, Mg II, Si II, C IV, and O VI in our simulations with observational data from Bordoloi et al. (2014), Werk et al. (2013), Tumlinson et al. (2013), Johnson et al. (2015), Tchernyshyov et al. (2022), Mishra et al. (2024), and Zheng et al. (2024). We exclude observational errors as they are $\approx \pm 0.01 - 0.15$ and are therefore negligible compared to the scale of the scatter of our

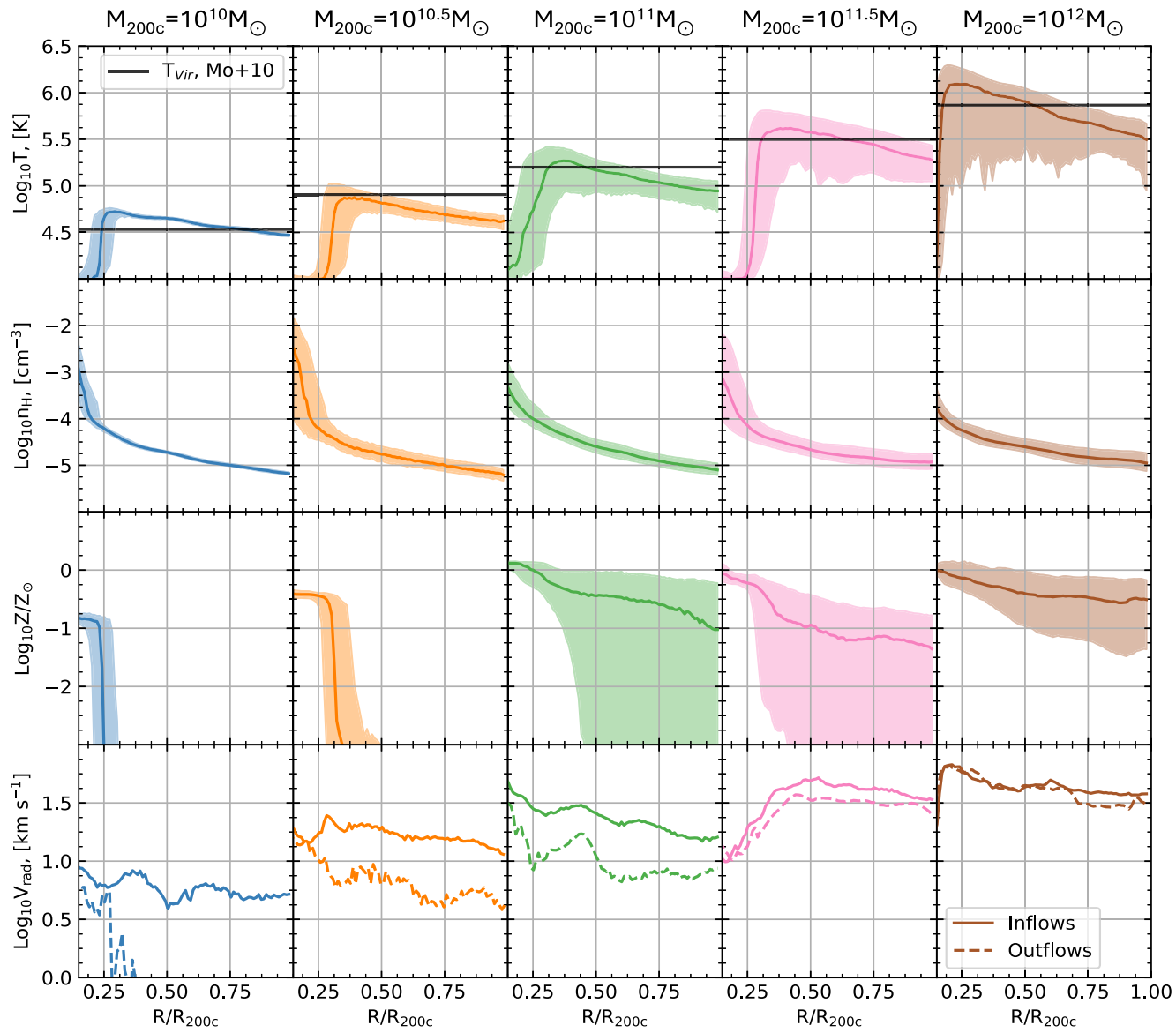

Figure 4. Median physical properties from top to bottom: temperature, density, metallicity, and radial velocity as a function of radius normalized by the virial radius from $0.15R_{200c}$ to R_{200c}. The shaded regions show the 16th and 84th percentile of the properties as a measure of the scatter for the haloes from Fig. 2. The halo mass increases from left to right, from 10^{10} to 10^{12} M$_\odot$ in steps of 0.5 dex and are the haloes halo10_0, halo10_9, halo11_0, halo11_4, and halo12_6 from Table 1. The temperature, metallicity, and radial velocity are mass-weighted, whereas the density is volume-weighted. The virial temperature for each halo is indicated by the solid black line in each panel of the temperature row. Gas associated with satellites and the ISM, i.e. the star-forming gas, has been excluded. The temperature profile decreases at $R > 0.3R_{200c}$ with a steeper decrease in more massive haloes. The metallicity is the highest in the centre in all haloes. Haloes with $M_{200c} \leq 10^{10.5}$ M$_\odot$ have a steep drop off at radii larger than $0.25R_{200c}$. For $M_{200c} > 10^{10.5}$ M$_\odot$, the metallicity profile is much shallower and the scatter is large. Reasonably metal-rich gas can be found in the outer CGM as well as metal-poor gas. Similar to Fig. 3, the density shows no strong dependence on halo mass, with a steep drop off in the inner $0.25R_{200c}$ CGM and a more shallow profile in the outer CGM. Finally, the outflows in $M_{200c} \leq 10^{11}$ M$_\odot$ haloes is significantly weaker than the inflowing matter. In more massive haloes, the inflows and outflows are at approximately equal rates.

simulations. The CGM is ionized via photoionization and collisional ionization. The level of ionization depends on the density and temperature of the gas, as well as the redshift (e.g. Strawn et al. 2023). We define two-temperature regimes: the warm regime which is traced by C IV and O VI at temperatures of $T = 10^{4.5}-10^{5.5}$ K, and a cool regime, traced by H I, Mg II, and Si II at temperatures of $T = 10^{4.0}-10^{4.5}$ K.

Fig. 5 shows halo projections oriented edge-on to the galactic stellar disc of, from left to right, $N_{\rm H\,I}$, $N_{\rm Mg\,II}$, $N_{\rm Si\,II}$, $N_{\rm C\,IV}$, and $N_{\rm O\,VI}$. Six different haloes – from top to bottom, halo10_11, halo10_9, halo10_2, halo11_2, halo11_5, and halo12_L8 (Table 1) – are chosen based on their stellar mass with values of $10^{8.3}$ M$_\odot$, $10^{8.8}$ M$_\odot$, $10^{9.3}$ M$_\odot$, $10^{9.7}$ M$_\odot$, $10^{10.1}$ M$_\odot$, and $10^{10.8}$ M$_\odot$, respectively. High column densities of H I and our metal ions are seen in the centres of these haloes. The low-ionization state ions highlight the filamentary structure of the outer CGM in the most massive haloes ($M_\star = 10^{10.8}$ M$_\odot$). We find low $N_{\rm C\,IV}$ and $N_{\rm O\,VI}$ in the outer CGM of galaxies with $M_\star \leq 10^{9.5}$ M$_\odot$ ($M_{200c} \leq 10^{11.0}$ M$_\odot$). $N_{\rm C\,IV}$ and $N_{\rm O\,VI}$ are higher in the outer CGM of more massive haloes, because these haloes contain higher temperature gas.

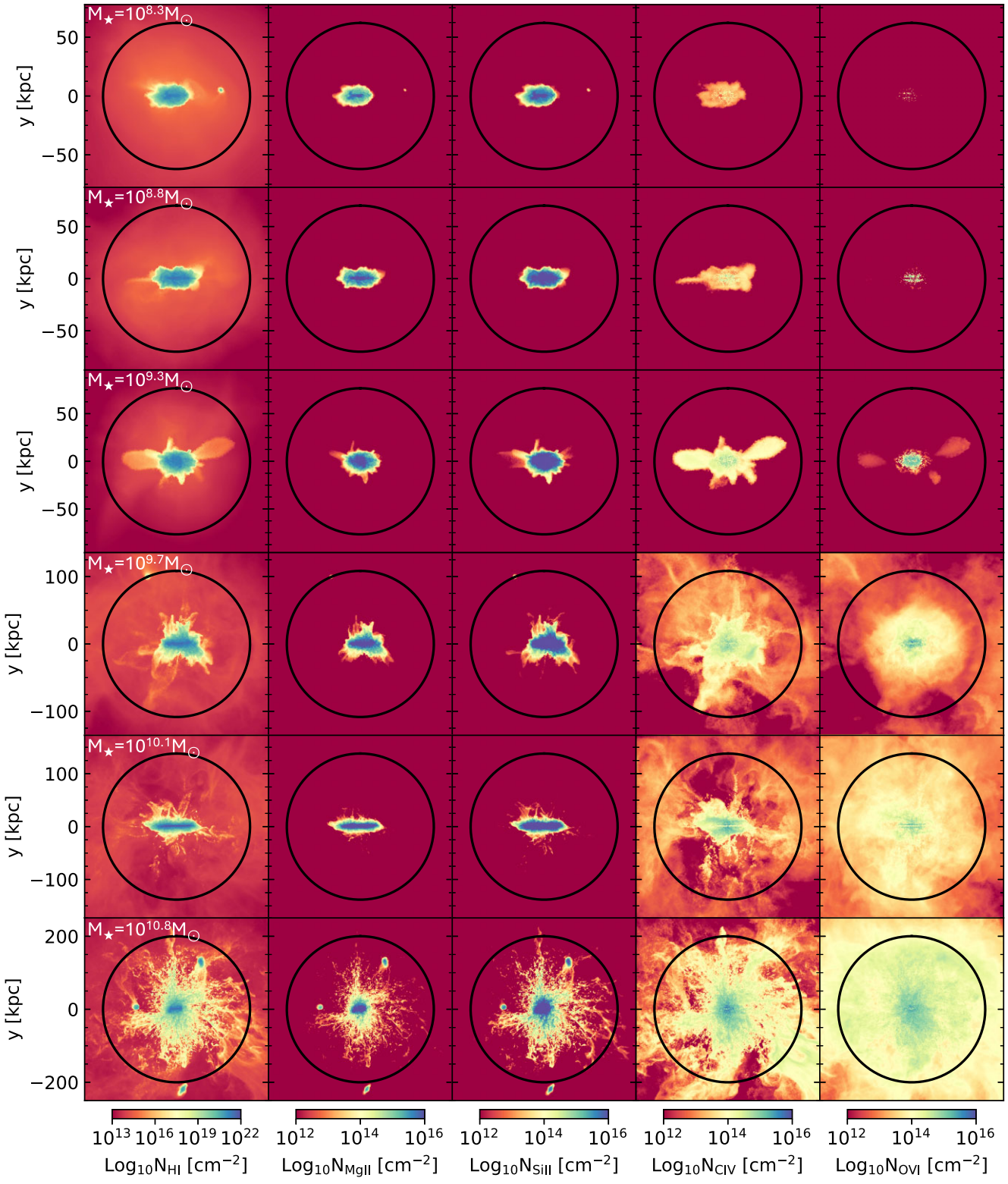

Figure 5. $2.5R_{200c} \times 2.5R_{200c}$ projections of six haloes – from top to bottom, halo10_11, halo10_9, halo10_2, halo11_2, halo11_5, and halo12_L8 (Table 1) – with a depth of $2R_{200c}$, rotated such that the stellar disc is edge-on. The chosen haloes are selected based on the stellar mass of the central galaxies and are thus different from those in Fig. 2. From top to bottom the stellar masses increase from $10^{8.3}$, $10^{8.8}$, $10^{9.3}$, $10^{9.7}$, $10^{10.1}$ to $10^{10.8}$ $M_\odot$. From left to right, columns correspond to H I, Mg II, Si II, C IV, and O VI. The virial radius is indicated by the black circle in each panel. Column densities are the highest in the centres of all haloes and decrease with radius. $N_{C\,IV}$ and $N_{O\,VI}$ increase with stellar mass, reaching high values even in the outer CGM.

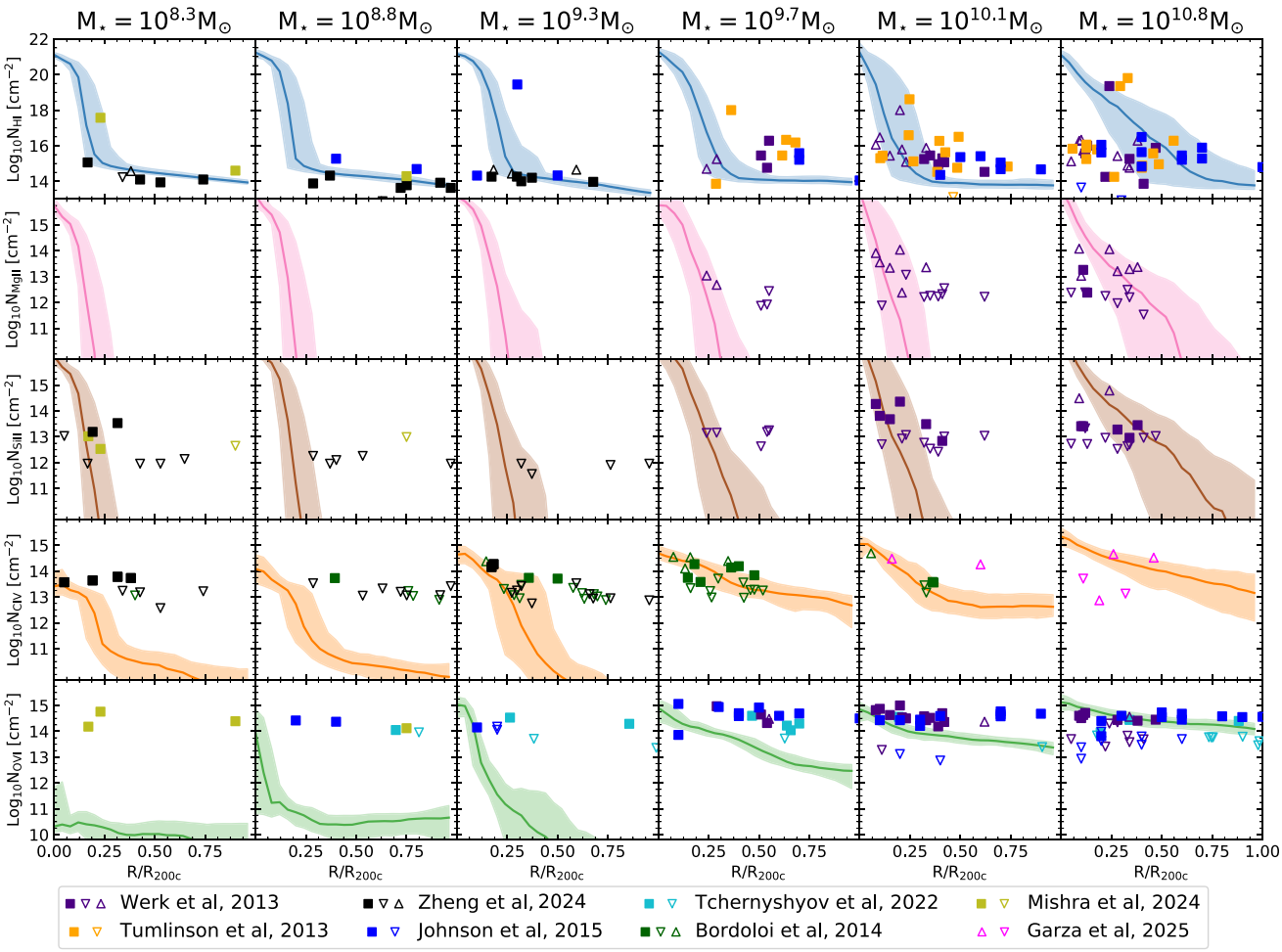

Figure 6. Radial profiles of H I and ion column densities, where the radius is normalized by R_{200c}, for the same haloes as in Fig. 5. The median is shown by solid curves and the 16th and 84th percentiles are shown as shaded regions. From top to bottom, each row shows the radial profile for $N_{\rm H\,I}$, $N_{\rm Mg\,II}$, $N_{\rm Si\,II}$, $N_{\rm C\,IV}$, and $N_{\rm O\,VI}$. Our radial profiles are compared with observational data from Werk et al. (2013), Tumlinson et al. (2013), Bordoloi et al. (2014), Johnson et al. (2015), Tchernyshyov et al. (2022), Mishra et al. (2024), Zheng et al. (2024), and Garza et al. (2025). These data are binned within $10^{8.0}$ M$_\odot$ $< M_\star <$ 10^{11} M$_\odot$ in equal intervals of 0.5 dex, increasing from left to right. The haloes included in this figure are halo10_11, halo10_9, halo10_2, halo11_2, halo11_5, and halo12_L8 (Table 1), and have stellar masses in the middle of these mass bins. Similarly to Fig. 7, gas associated with the ISM is not included in this figure. The column density of all ions increases with stellar mass in the outer CGM. Our column density for H I agrees with most observational detections in haloes with $M_\star < 10^{9.7}$ M$_\odot$. We see underpredictions at radii $R > 0.5R_{200c}$ for $10^{9.7}$ and $10^{10.1}$ M$_\odot$, and an overprediction at low radii at $M_\star = 10^{10.8}$ M$_\odot$. C IV agrees with observations at small radii ($R < 0.4R_{200c}$) for $M_\star \geq 10^{9.3}$ M$_\odot$, while O VI is slightly underproduced at all stellar masses except the most massive ($M_\star = 10^{10.8}$ M$_\odot$). Mg II and Si II follow similar radial profiles with sharp drop off between $\sim 0.2R_{200c}$and $0.3R_{200c}$. There are few observational detections below $10^{10.1}$ M$_\odot$ to compare with our column densities. We do however find reasonable agreement with observations in the two most massive haloes studied.

In this section, we analyse $N_{\rm H\,I}$, $N_{\rm Mg\,II}$, $N_{\rm Si\,II}$, $N_{\rm C\,IV}$, and $N_{\rm O\,VI}$ as functions of radius (Fig. 6) and stellar mass (Fig. 7). We conclude our analysis by measuring the ion mass-weighted physical properties as a function of halo mass (Fig. 8).

4.1 Radial profiles of column density

Fig. 6 shows the dependence of the median and 16th and 84th percentiles for, from top to bottom, $N_{\rm H\,I}$, $N_{\rm Mg\,II}$, $N_{\rm Si\,II}$, $N_{\rm C\,IV}$, and $N_{\rm O\,VI}$ on 2D radius, or impact parameter, compared with observational data. We binned the observational data by stellar mass between $10^8$and 10^{11} M$_\odot$ in equal intervals of 0.5 dex from left to right. We show the same simulated haloes as in Fig. 5, which have a stellar mass that is as close to the middle of the stellar mass bin as possible. We calculate the radial column density profiles by taking the median line-of-sight column density and its percentiles in 25 bins from the centre of the CGM out to the virial radius.

Our $N_{\rm H\,I}$ shows a steep decrease from $\sim 0.1R_{200c}$ to $\sim 0.3R_{200c}$. The scatter of $N_{H\,I}$ is similar for all haloes up to $10^{10.8}$ M$_\odot$ in the inner $0.3R_{200c}$. At larger impact parameters ($R > 0.3R_{200c}$), the column density exhibits a shallow decrease out to the virial radius for all haloes up to and including $10^{10.1}$ M$_\odot$. At a stellar mass of $10^{10.8}$ M$_\odot$, we see significantly wider scatter beyond $0.3R_{200c}$ and shallower decrease than at lower stellar masses out to $\sim 0.7R_{200c}$. The $N_{\rm H\,I}$ in observations is fairly constant between a stellar mass of $10^{8.3}-10^{9.3}$ M$_\odot$, matching our simulated radial profiles at $\sim 10^{14}$cm^{-2}. For $10^{9.7}$ M$_\odot \leq M_\star \leq 10^{10.1}$ M$_\odot$, our simulations underpredict $N_{\rm H\,I}$ outside of $0.5R_{200c}$ and match at smaller impact parameters. At $10^{10.8}$ M$_\odot$, we see better agreement between $0.25R_{200c}$ and $0.75R_{200c}$ and observations but an overprediction at $R < 0.25R_{200c}$.

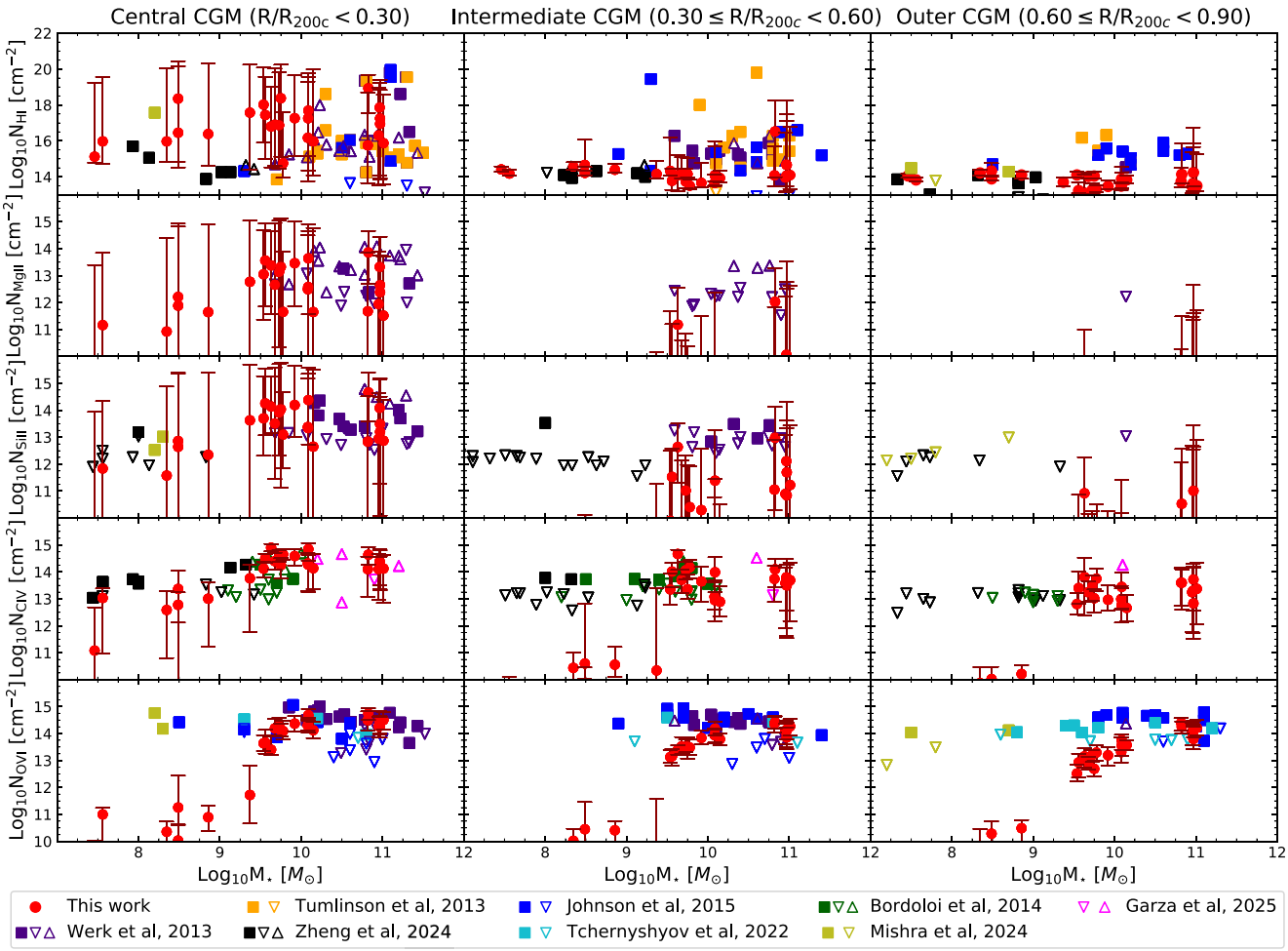

Figure 7. Simulated and observed column densities as a function of $M_\star$. From top to bottom, the red circles show the median of $N_{\rm H\,I}$, $N_{\rm Mg\,II}$, $N_{\rm Si\,II}$, $N_{\rm C\,IV}$, and $N_{\rm O\,VI}$ with 16$^{\rm th}$ and 84$^{\rm th}$ percentile scatter bars. We separate the column densities within $0.9R_{\rm 200c}$ in three radial bins with widths of $0.2R_{\rm 200c}$ and of $0.3R_{\rm 200c}$. The depth of the projection is $2R_{\rm 200c}$ and the median is measured along two orthogonal edge-on directions. We compare with observational data from Werk et al. (2013), Tumlinson et al. (2013), Bordoloi et al. (2014), Johnson et al. (2015), Tchernyshyov et al. (2022), Mishra et al. (2024), Zheng et al. (2024), and Garza et al. (2025). Detections are shown as filled squares and upper (lower) limits as empty downwards (upwards) arrows. The observational error bars are omitted for readability. Additionally, cells associated with the ISM are removed from our measurements to select only CGM gas of the main halo. The column density of warm ions (C IV and O VI) is high above $10^{9.5}$ M$_\odot$ stellar mass haloes for all radial bins. C IV is relatively constant above $M_\star = 10^{9.5}$ M$_\odot$ and agrees with detections at all radii for higher mass haloes and in lower mass haloes within $0.2R_{\rm 200c}$. Lower mass systems have significantly lower column densities, especially at larger radii. O VI broadly agrees with observations for $M_\star > 10^{9.5}$ M$_\odot$ at multiple radii, while lower mass systems show $N_{\rm O\,VI}$ values roughly ∼3 dex lower. The cool regime (H I, Mg II, and Si II) has high column density in the centre for all haloes but drops off significantly above $0.2R_{\rm 200c}$. $N_{\rm Mg\,II}$ and $N_{\rm Si\,II}$ are higher in systems with $M_\star > 10^{9.5}$ than in lower mass systems at large radii. H I has larger scatter in more massive haloes but no significant dependence of the median $N_{\rm H\,I}$ on stellar mass.

For Mg II and Si II, the column densities at impact parameters $< 0.2R_{\rm 200c}$ are high, with a steep decrease between $0.2R_{\rm 200c}$ and $0.3R_{\rm 200c}$ for $M_\star \leq 10^{10.1}$ M$_\odot$. We notice a shallower decrease in median and an increase in scatter for both of these ions for $M_\star = 10^{10.8}$ M$_\odot$, similar to $N_{\rm H\,I}$.

Data for stellar masses $\leq 10^{9.7}$ M$_\odot$ are fairly sparse, leading to a lack of detections to compare with. Above $10^{10.1}$ M$_\odot$, we find good agreement with detections in the inner $0.25R_{\rm 200c}$ for $N_{\rm Si\,II}$. At $M_\star = 10^{10.8}$ M$_\odot$, we see an overprediction at small impact parameters for both Mg II and Si II. We find that our simulations match detections beyond a impact parameter of $0.25R_{\rm 200c}$ for Si II.

The column densities of C IV and O VI steeply decrease with impact parameter for $M_\star \leq 10^{9.3}$ M$_\odot$. $N_{\rm C\,IV}$ and $N_{\rm O\,VI}$ are higher in the outer CGM in haloes with $M_{\rm 200c} \geq 10^{11}$ M$_\odot$ or $M_\star \geq 10^{9.7}$ M$_\odot$. This is likely because of stronger outflows, and because the gas in these haloes has a higher virial temperatures than in smaller haloes. This means there will be more gas at 10^5–$10^{5.5}$ K where C IV and O VI is commonly found.

We see good agreement for $N_{\rm C\,IV}$ with observations in our $10^{9.7}$ M$_\odot$ stellar mass halo. For $M_\star = 10^{10.1}$ M$_\odot$, we find agreement with the limited data available.

There are few detections of $N_{\rm O\,VI}$ at stellar masses below $10^{9.3}$ M$_\odot$. Our dwarf simulations predict no detectable absorption associated with haloes outside the very centre of these haloes likely a combination of low metallicity because of weak outflows and low temperatures. For $M_\star = 10^{9.7}$ M$_\odot$ and $M_\star = 10^{10.1}$ M$_\odot$, our simulations underpredict $N_{\rm O\,VI}$ in most observations except in the inner CGM. At these stellar masses, the $N_{\rm O\,VI}$ decreases with radius

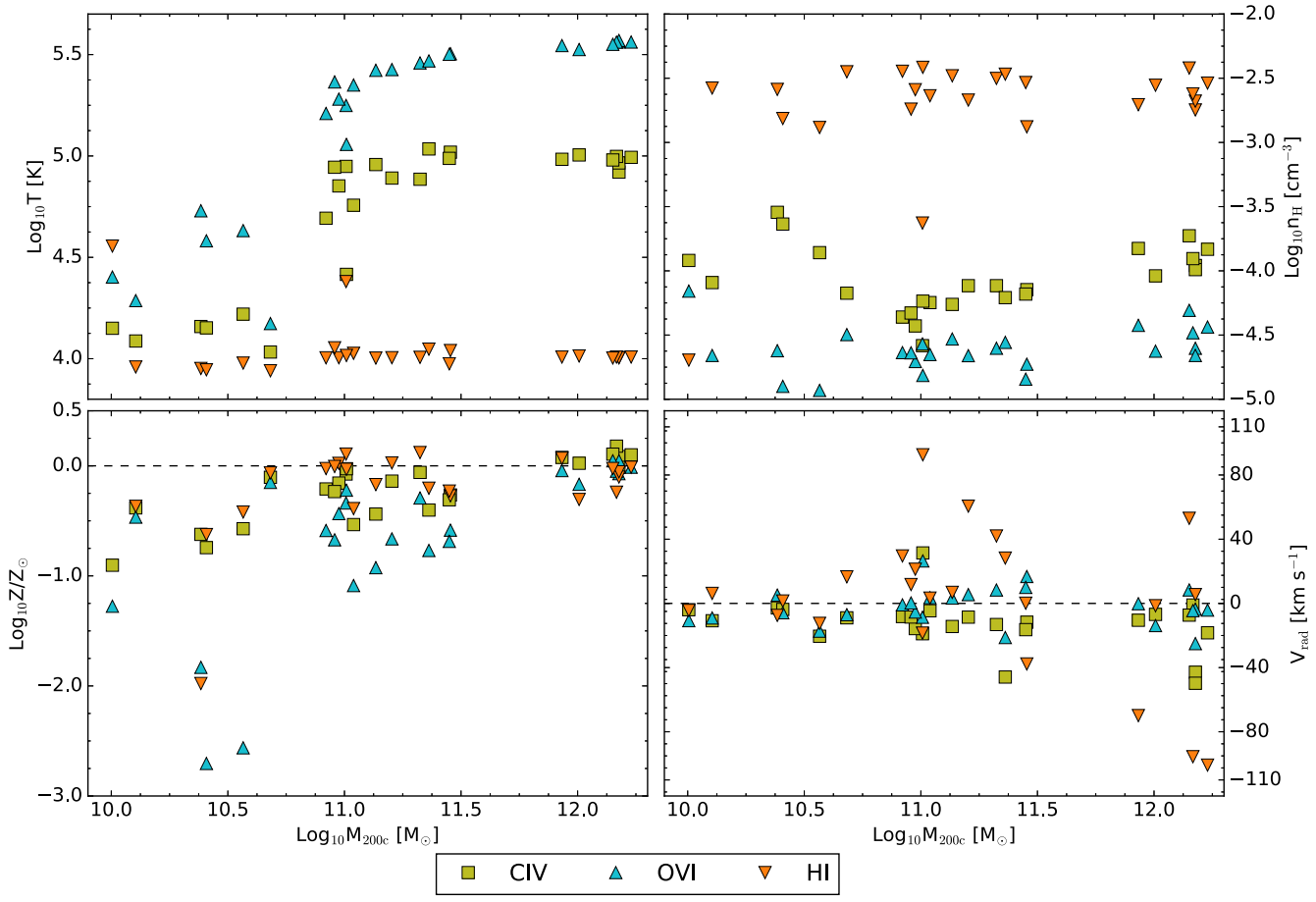

Figure 8. Temperature (top, left), hydrogen number density (top, right), metallicity (bottom, left), and radial velocity (bottom, right) against M_{200c} as in Fig. 3. We show the median values weighted by the ion mass of C IV (yellow squares), O VI (blue upward triangles), and H I (orange downward triangles) and measured in the range $0.3 \leq R/R_{200c} \leq 1.0$. Because H I, Mg II, and Si II are all similar, we omit the metal ions and show only H I for clarity. We see a sharp increase in temperature of O VI and C IV at $M_{200c} = 10^{11}$ M$_\odot$, indicating a transition from PIE to CIE. The metallicity is higher in more massive haloes for all ions. The density and radial velocity show no significant dependence on halo mass. There are significant differences between the temperature, the density, the metallicity, and the radial velocity of these ions. H I remains at 10^4 K for all haloes, at relatively high densities. C IV and O VI trace higher temperatures up to 10^5 and $10^{5.5}$K, respectively, in more diffuse gas, which explains its ubiquity in the final three rows of Fig. 5.

more steeply than observations indicate. At $10^{10.8}$ M$_\odot$, we find the best agreement with detections from observations, but our median and scatter lie above most upper limits.

4.2 Column density and stellar mass

Fig. 7 shows the various column densities as a function of stellar mass. The median is shown as red circles and the scatter is quantified with 16$^{\text{th}}$ and 84$^{\text{th}}$ percentiles and shown as scatter bars. The median and percentiles are calculated along two orthogonal axes for which the central galaxy has been rotated to be edge-on. We split these data into three radial bins of $0.1R_{200c}-0.3R_{200c}$ (inner CGM), $0.3R_{200c}-0.6R_{200c}$ (intermediate CGM), and $0.6R_{200c}-0.9R_{200c}$ (outer CGM). Observational detections are shown as filled squares, upper limits as open downward arrows, and lower limits as open upward arrows. We additionally set the ion fraction to zero in the ISM. We calculate the median column density as a function of stellar mass by taking the median line-of-sight column density and the 16$^{\text{th}}$ and 84$^{\text{th}}$ percentiles within the stellar mass bins given above.

The median and scatter of $N_{\text{H I}}$ decreases with radius for all stellar masses. In the inner CGM, our median $N_{\text{H I}}$ slightly overpredicts observations for $M_\star \leq 10^{9.5}$ M$_\odot$, whereas higher stellar mass haloes exhibit medians and large scatter that agree with observational data. The large scatter in the inner CGM can be attributed to the decrease in the $N_{\text{H I}}$ radial profile as seen in Fig. 6. The median $N_{\text{H I}}$ in the intermediate CGM decreases to $\sim 10^{13.5}$–$\sim 10^{14.5}$cm^{-2} where we find that the median and scatter agree reasonably well with observations. In the outer CGM, most observational data at $M_\star > 10^9$ M$_\odot$ are somewhat higher than our median column densities for H I. Most $N_{\text{H I}}$ detections are within the upper percentile of our scatter above a stellar mass of 10^{10} M$_\odot$.

The median $N_{\text{Mg II}}$ and $N_{\text{Si II}}$ follow a similar trend to H I for all stellar masses: an overprediction compared to the observational data in the inner CGM and a decrease with radius, which leads to values more in agreement with observations. Median column densities range from 10^{11} to $\sim 10^{14}$ cm^{-2} in the inner CGM and match observational detections and limits. The upper percentiles of our $N_{\text{Si II}}$ results fall within the observed values and upper limits for $M_\star > 10^{9.5}$ M$_\odot$ in the intermediate CGM and underpredict observations at all stellar masses

in the outer CGM. The median $N_{\rm Mg\,II}$ is typically ∼1 dex lower than a systems Si II and underpredicts observations in the intermediate CGM. This is partially due to the underproduction of Mg following the yield set of Portinari et al. (1998), which underproduces Mg by a factor of ∼2. The outer CGM for Mg II has too few observations to do robust comparisons. For $M_\star \leq 10^{9.5}$ M$_\odot$, $N_{\rm Mg\,II}$ and $N_{\rm Si\,II}$ decrease to values that would be undetectable in observations.

We find that the $N_{\rm C\,IV}$ is consistent with observations in the inner CGM. $N_{\rm C\,IV}$ increases with stellar mass up to $10^{9.5}$ M$_\odot$ beyond which the column density remains constant. The median $N_{\rm C\,IV}$ decreases and its scatter increases with increasing radii. The most significant change in $N_{\rm C\,IV}$ is seen in haloes with $M_\star \leq 10^{9.5}$ M$_\odot$: the median $N_{\rm C\,IV}$ decreases by ∼2.5 dex from $N_{\rm C\,IV} \approx 10^{13}$ cm^{-2} to $N_{\rm C\,IV} \approx 10^{10.5}$ cm^{-2} in the transition from the inner to the intermediate CGM. This is below observational detections for $M_\star \leq 10^{9.5}$ M$_\odot$. Some of the median $N_{\rm C\,IV}$ in the outer CGM decrease further but there is no increase in these low-mass haloes $N_{\rm C\,IV}$. For $M_\star > 10^{9.5}$ M$_\odot$, $N_{\rm C\,IV}$ decreases by ∼1.5 dex from the inner to the outer CGM and largely agrees with observations.

Our $N_{\rm O\,VI}$ agrees with observational detections for $M_\star > 10^{9.5}$ M$_\odot$ in the inner CGM. The median $N_{\rm O\,VI}$ decreases by $\sim 0.5-1$ dex from the inner CGM ($N_{O\,VI} = 10^{13.5} - 10^{14.5}$ cm^{-2}) to the intermediate CGM ($N_{O\,VI} = 10^{12.5} - 10^{14}$ cm^{-2}) at these stellar masses. From the inner to the outer CGM, the median $N_{O\,VI}$ decreases by ∼1 dex in systems with stellar masses of $10^{9.5} \leq M_\star < 10^{10.5}$ M$_\odot$, whereas $N_{O\,VI}$ in systems with stellar mass $M_\star \approx 10^{11}$ M$_\odot$ only decreases by ∼0.5 dex. For $M_\star \leq 10^{9.5}$ M$_\odot$, the median $N_{\rm O\,VI}$ is $\sim 3-4$ dex lower than in more massive systems. The scatter in $N_{\rm O\,VI}$ is small for $M_\star > 10^{9.5}$ M$_\odot$ but larger at low masses. For all radial bins, $N_{\rm O\,VI}$ is substantially higher above $10^{9.5}$ M$_\odot$.

4.3 Relation to physical properties

To better understand the properties of gas that give rise to these absorption line features, Fig. 8 shows the physical properties as in Fig. 3 weighted by the mass of C IV (yellow squares), O VI (blue upward triangles), and H I (orange downward arrows). This is to highlight the physical properties traced by the ions we have selected. Mg II- and Si II-weighted values are not shown for clarity, but show similarities to the H I-mass-weighted properties. We computed the ion-weighted median values of these properties in the range $0.3 \leq R/R_{\rm 200c} \leq 1.0$. This excludes the central CGM, containing primarily cool relatively dense metal-rich and mostly inflowing gas.

We see gas traced by O VI at higher temperatures than C IV, and gas traced by H I is the coolest, as we would expect for lower ionization states. We see a distinct change in temperature at $M_{\rm 200c} = 10^{11}$ M$_\odot$, for O VI and C IV. Their temperature increases by ∼0.7 dex, corresponding to their CIE values (see e.g. Strawn et al. 2023). We find that the temperature (density) of C IV and O VI lies around $\sim 10^5$ K ($\sim 10^{-4}$ cm^{-3}) and $\sim 10^{5.5}$ K ($\sim 10^{-4.8}$ cm^{-3}), respectively, for $M_{\rm 200c} > 10^{11}$ M$_\odot$.

H I, and Mg II and Si II are found consistently at low temperatures of $\sim 10^4$ K. The densities of the gas probed by these low ionization state ions range from $\sim 10^{-3.5}$ to $\sim 10^{-2.5}$ cm^{-3} independent of mass. These ions populate the coolest and densest parts of the outer 70 per cent of the CGM. Additionally, Fig. 5 shows H I, Mg II, and Si II in a largely filamentary structure in the most massive halo. By comparing to the most massive halo in Fig. 2, we can see that filaments found in the halo are at cooler temperatures and higher densities than the rest of the halo, indicating H I, Mg II, and Si II trace cool and dense filamentary structure.

The metallicity of the gas traced by C IV, O VI, and H I is higher in more massive haloes. C IV and H I trace higher metallicity gas than O VI at fixed halo mass. This is because O VI traces more diffuse gas, which is typically more metal-poor. Above $\gtrsim 10^{12}$ M$_\odot$, all ions are tracing approximately solar metallicity gas.

We find that the ion-weighted radial velocity does not show a strong dependence on halo mass. The median O VI radial velocity has no preferred direction and is divided equally between slightly inflowing and slightly outflowing gas, while the median C IV is inflowing for most of our haloes. H I primarily traces outflowing gas at intermediate halo masses ($10^{10.5}-10^{11.5}$ M$_\odot$). Mg II shows near identical properties to H I. Mg II has previously been found to be dominated by inflows in the inner 60 kpc of $10^{11.5}-10^{12}$ M$_\odot$ haloes (DeFelippis et al. 2021). Interestingly, we additionally analysed the median radial velocity of Mg II and found inflows dominating above $10^{11.5}$ M$_\odot$ in the outer 70 per cent of the CGM. However, due to the issues with the Mg II yield as discussed earlier, it may be unwise to make assumptions about the inflowing and outflowing Mg II gas.

5 CONCLUSION

5.1 Summary

We have investigated the role the halo mass plays in changing the physical properties of the CGM in the Auriga suite of cosmological simulations. This included an analysis of the temperature, density, metallicity, and radial velocity of the CGM for halo masses in the range $10^{10}-10^{12}$ M$_\odot$. We additionally analysed the column density of H I and the metal ions C IV, O VI, Mg II, and Si II as a function of stellar mass and radius, and compared to observational data. While this is for one galaxy formation model only, it can give us an idea of what to expect in future observations and can additionally be used to constrain models.

We summarize the results of our study below:

(i) The CGM of dwarf galaxies (∼10^{10} M$_\odot$) features a narrow radial temperature range. The scatter, defined as the range between the 16$^{\rm th}$ and 84$^{\rm th}$ percentile of our data, in temperature increases from ∼0.5 dex in 10^{10} M$_\odot$ haloes to ∼1.5 dex in 10^{12} M$_\odot$ haloes. This indicates the multiphase nature of the CGM is dependent on the halo mass (Fig. 3).

(ii) The median and scatter of the volume-weighted density shows no clear dependence on halo mass. The scatter of the mass-weighted density does show some increase with halo mass (Fig. 4).

(iii) The CGM of all of our simulated dwarf galaxies is extremely metal-deficient at large radii. This is due to weak outflows up to a halo mass of 10^{11} M$_\odot$. The metallicity in the centre of the CGM of these haloes is high but does not reach solar values. The scatter in metallicity is large from halo-to-halo with metallicities ranging from less than 10^{-5} Z$_\odot$ up to $10^{-0.5}$ Z$_\odot$. Haloes with masses of the order of ∼10^{12} M$_\odot$ reach solar to supersolar metallicities in their centres, and have significantly more metal-enriched gas than dwarfs at large radii and exhibit large scatter in metallicity. Most of the gas in Milky Way-mass haloes reaches metallicities between 10 and 100 per cent solar, though there are some lower metallicities above $0.5R_{\rm 200c}$ (Figs 3 and 4).

(iv) We found low outflow velocities in our dwarf galaxies, which means that gas is not efficiently transported out of the intermediate CGM to larger radii. The gas inflow velocities around dwarf galaxies are much higher. The inflow and outflow velocities increase with halo mass. Above halo masses of ∼$10^{11.5}$ M$_\odot$, the inflow and outflow velocities are roughly equal out to at least the virial radius (Fig. 3).

(v) The median column densities of our cool regime (H I, Mg II, and Si II) are significantly higher than column densities derived from observations in the inner $0.2R_{200c}$. $N_{\rm H\,I}$ decreases to between 10^{14} and 10^{15} cm^{-2} at $0.6R_{200c}$, in reasonable agreement with observations. $N_{\rm Mg\,II}$ and $N_{\rm Si\,II}$ drop off sharply outside of $0.2R_{200c}$ at stellar masses $M_\star \leq 10^{10}$ M$_\odot$ (Fig. 7). There are not enough observational detections to compare to for Si II below $10^{9.5}$ M$_\odot$. Above $10^{9.5}$ M$_\odot$, we find reasonable agreement with detections of Si II out to $0.4R_{200c}$ and upper limits at larger radii (Fig. 6).

(vi) The median column density of C IV agrees with observational detections for $R < 0.2R_{200c}$ in all our simulated haloes. $N_{\rm C\,IV}$ decreases at larger radii for all haloes, but shows a very steep decrease in $M_\star < 10^{9.5}$ M$_\odot$ systems, below the few available detections between $0.2R_{200c}$ and $0.4R_{200c}$. The median $N_{\rm O\,VI}$ largely matches observations at high stellar masses (above $10^{9.5}$ M$_\odot$) but underpredicts them for stellar masses below $10^{9.5}$ M$_\odot$ (Fig. 7). The column densities of both C IV and O VI in haloes above a stellar mass of $10^{9.5}$ M$_\odot$ decrease by ∼1 dex on average from the centre out to $\sim 0.6R_{200c}$, which is not seen in observations (Fig. 6).

(vii) We investigated the properties of gas probed by C IV, O VI, and H I at radii greater than $0.3R_{200c}$ and found that each ion corresponds to its CIE temperature of 10^5, $10^{5.5}$, and 10^4 K, respectively (e.g. fig. 2 from Strawn et al. 2023). A clear transition from PIE to CIE for C IV and O VI is seen at a halo mass of 10^{11} M$_\odot$, featuring a temperature increase from $\sim 10^{4.1}$ to $\sim 10^5$ K for C IV and $\sim 10^{4.5}$ to $\sim 10^{5.5}$ K for O VI. H I is found in gas that is consistently cool ($\sim 10^4$ K) and at densities between $\sim 10^{-3.5}$ and 10^{-2} cm^{-3}. The ion-weighted metallicity shows that H I and C IV reside in higher metallicity gas than O VI for all haloes up to 10^{12} M$_\odot$. The ion-weighted radial velocity shows mostly outflowing H I and inflowing O VI gas between halo masses of $10^{10.5}$ and $10^{11.5}$ M$_\odot$. For halo masses greater than $10^{11.5}$ M$_\odot$, all metal ions we investigated are preferentially associated with inflowing gas likely tracing large-scale fountain flows (Fig. 8).

5.2 Resolution test

Fig. 9 shows this, comparing the temperature, density, metallicity, and radial velocity of the main central haloes at different mass resolutions: $\sim 8 \times 10^2$ M$_\odot$ (extra high resolution) and $\sim 5.4 \times 10^4$ M$_\odot$ (standard resolution). The extra high-resolution simulations have halo masses $\lesssim 10^{10.5}$ M$_\odot$, the level 3 simulations ('high' resolution) probe halo masses between 10^{10} and 10^{12} M$_\odot$, and the standard resolution simulations have halo masses $\geq 10^{11}$ M$_\odot$ and $\lesssim 10^{12}$ M$_\odot$.

We find no significant differences between each mass resolution. Our resolution tests show similar scatter across the physical properties studied, irrespective of the resolution of the simulation. Across our three resolution levels, or a factor of 64 in mass resolution, we see the same trends for the CGM properties as a function of halo mass. Additionally, the median and scatter of the column density of all our ions does not change significantly with resolution (not shown).

5.3 Comparison with prior literature

A similar study by Hani et al. (2019) studied the haloes of 40 L* galaxies in Auriga with stellar mass between $10^{10.3}$ and $10^{11.1}$ M$_\odot$. They found that the gas and metal content of the CGM show a tight correlation with the stellar mass of the host galaxy. Contrarily, they found the ionization of metals in the CGM is independent of stellar mass. This seems contradictory to what we find – haloes of increasing stellar mass exhibit higher column densities for H I, Si II, and O VI.

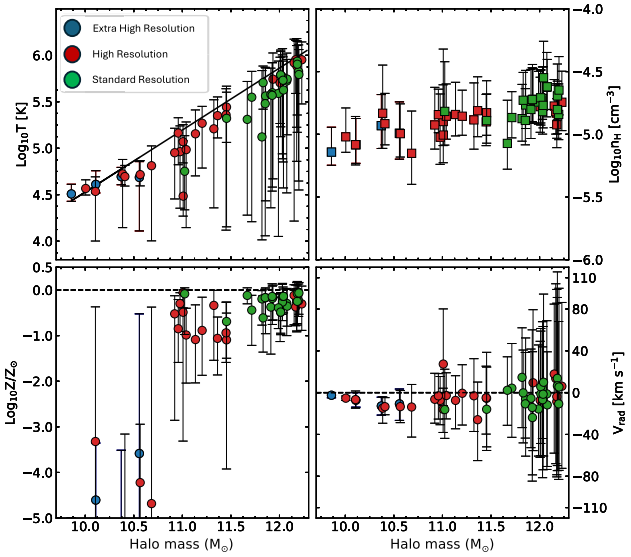

Figure 9. A resolution test of, in clockwise order starting at the top left, temperature, density, metallicity, and radial velocity at three different resolution levels: 8×10^2 M$_\odot$ (blue), 5.4×10^3 M$_\odot$ (red), and 6×10^4 M$_\odot$ (green). The haloes in red are those used in the rest of this work. We show an additional 12 simulations of a subset of these haloes at eight times lower mass resolution and four simulations at eight times higher mass resolution. The temperature, metallicity, and radial velocity are mass-weighted while the density is volume-weighted. We find similar trends in the median values regardless of mass resolution for all physical properties.

However, this may be explained by the smaller stellar mass range ($2.1 \leq M_\star[10^{10}\,{\rm M}_\odot] \leq 11.7$) and halo mass range ($0.5 \leq M_\star[10^{12}\,{\rm M}_\odot] \leq 2.0$) of Hani et al. (2019). Our results show that for a much larger range of stellar masses the column density changes in both median and scatter specifically for high-ionization states such as C IV and O VI.

In a different suite of simulations, called NIHAO (Wang et al. 2015), Gutcke et al. (2017) analysed a set of simulations with halo mass similar to our own of $10^{9.7}$–$10^{12.5}$ M$_\odot$ investigating the column density of H I and O VI. Using the same self-shielding approximation as our simulations (Rahmati et al. 2013), they found better agreement between their H I column densities and observations than for O VI. Additionally, Gutcke et al. (2017) show that the trend of O VI with luminosity (a proxy for stellar mass) in their simulations agrees with observations but their radial dependence of O VI underpredicts the observations. In comparison to our work, the column density of H I follows a similar trend as a function of impact parameter reaching a plateau of $\sim 10^{14}$ cm^{-2}. We find lower O VI column densities than Gutcke et al. (2017) out to the virial radius in haloes with $M_{200c} < 10^{11}$ M$_\odot$. At higher halo masses, Gutcke et al. (2017) find the radial dependence of O VI has a narrow range of values between 10^{13} and 10^{14} cm^{-2}. We find column densities higher than this, extending to the virial radius.

Hummels et al. (2013) conducted similar work investigating the column density of H I, Si II, C IV, and O VI in the CGM of a Milky Way-mass galaxy with different stellar feedback prescriptions. They find that even minimal feedback can still push metals out to large radii (> 50 kpc) but there is a lack of multiphase gas that underproduces observed ions – this is notably true of O VI which did not match any of their models. This is different to our results, which show column densities of O VI in Milky Way-mass haloes that better match observations at large radii. They additionally found that increasing

thermal feedback from the galaxy to very high values increased the $N_{\rm O\,VI}$ but still underpredicted observations.

Similar underpredictions for O VI and H I were found in the FIRE-2 suite of MHD simulations from Ji et al. (2020) who found that adding cosmic ray feedback in Milky Way-mass haloes increased columns in line with observational detections and limits.

In order to compute the column density in our simulations, we calculated the metal ion mass fraction in post-processing based on tables generated by Hummels et al. (2017) using CLOUDY (Ferland et al. 2017). Producing mock spectra for these simulations utilizing post-processing tools such as TRIDENT (Hummels et al. 2017) would allow us to bring our simulation analysis closer to observational data instead of comparing to derived quantities. Hafen et al. (2024) used TRIDENT to compare synthetic absorption spectra from three different simulation sets. They found reasonable agreement between the density, temperature, and metallicity derived from synthetic absorption spectra of uniform clouds and multicloud systems, and the source properties used to generate synthetic absorption spectra to within 0.1 dex. Mock spectra would provide us with a more robust method of comparison between observations and simulations and increase the amount of observational data we can use.

Furthermore, previous studies have shown that background or foreground absorbers may be incorrectly attributed to a halo if their line-of-sight velocity falls within the observational velocity range, usually ± 500 km s^{-1}, while the gas originates from different haloes outside of the virial radius (Ho, Martin & Schaye 2020; Weng et al. 2024). Our column densities were measured along a restricted line-of-sight depth of $2R_{\rm 200c}$. This could potentially account for discrepancies between our column densities and the observations we compared with, as Weng et al. (2024) find that larger radii from the centre increases the line-of-sight contribution from satellites, other haloes and the IGM.

Our results likely depend on specific modelling choices in the Auriga galaxy formation model. Varying certain aspects of our simulations in the future will help to better determine how sensitive our results are to these changes. Specifically, we are referring to relevant subgrid model variations such as an alternative kinetic AGN feedback model and additional feedback from cosmic rays, which is likely important in low-mass haloes, which are dominated by stellar feedback (Dashyan & Dubois 2020), an improved ISM model that incorporates multiphase gas physics, and a stellar feedback model that is more efficient in dwarf galaxies. Furthermore, the comparisons between observations and our simulations have shown that there are some underpredictions in the column density of low-mass haloes. It may be worth including alternative methods of calculating column density such as using a post-processing code like TRIDENT (Hummels et al. 2017) to produce synthetic absorption line spectra that can be compared to observations. Comparisons between CGM predictions and observables are a promising way forward to constrain and distinguish between different galaxy formation models. Additional physical processes such as incorporating cosmic ray feedback in simulations have shown that outflow rates in dwarf galaxies increase and agree more with observations (Farcy et al. 2022; Butsky et al. 2024; DeFelippis et al. 2024).

ACKNOWLEDGEMENTS

We would like to thank the referee for their useful comments on the paper. FvdV is supported by a Royal Society University Research Fellowship (URF\R\241005). RG acknowledges financial support from an STFC Ernest Rutherford Fellowship (ST/W003643/1). Software used for this work includes NUMPY (Harris, Millman & van der Walt 2020) and MATPLOTLIB (Hunter 2007). The simulations were performed on computing resources provided by the Max Planck Computing and Data Facility in Garching.

DATA AVAILABILITY

The Auriga suite of cosmological simulations, including all simulations used in this work, is available at the following website https://wwwmpa.mpa-garching.mpg.de/auriga/dataspecs.html. The absorption line tables used in this study are part of the TRIDENT project and are available at the following website https://trident-project.org/data/ion_table/.

REFERENCES

Agertz O. et al., 2020, MNRAS, 491, 1656
Anand A., Nelson D., Kauffmann G., 2021, MNRAS, 504, 65
Appleby S., Davé R., Sorini D., Storey-Fisher K., Smith B., 2021, MNRAS, 507, 2383
Behroozi P. S., Wechsler R. H., Conroy C., 2013, ApJ, 770, 57
Bordoloi R. et al., 2014, ApJ, 796, 136
Butsky I. S., Hopkins P. F., Kempski P., Ponnada S. B., Quataert E., Squire J., 2024, MNRAS, 528, 4245
Dashyan G., Dubois Y., 2020, A&A, 638, A123
Davis M., Efstathiou G., Frenk C. S., White S. D. M., 1985, ApJ, 292, 371
DeFelippis D., Bouché N. F., Genel S., Bryan G. L., Nelson D., Marinacci F., Hernquist L., 2021, ApJ, 923, 56
DeFelippis D., Bournaud F., Bouché N., Tollet E., Farcy M., Rey M., Rosdahl J., Blaizot J., 2024, MNRAS, 530, 52
Farcy M., Rosdahl J., Dubois Y., Blaizot J., Martin-Alvarez S., 2022, MNRAS, 513, 5000
Faucher-Giguère C.-A., Lidz A., Zaldarriaga M., Hernquist L., 2009, ApJ, 703, 1416
Ferland G. J. et al., 2017, Rev. Mex. Astron. Astrofis., 53, 385
Fox A. J., Wakker B. P., Savage B. D., Tripp T. M., Sembach K. R., Bland-Hawthorn J., 2005, ApJ, 630, 332
Frenk C. S., White S. D. M., Davis M., Efstathiou G., 1988, ApJ, 327, 507
Garza S. L., Werk J. K., Berg T. A. M., Faerman Y., Oppenheimer B. D., Bordoloi R., Ellison S. L., 2025, ApJ, 978, L12
Girelli G., Pozzetti L., Bolzonella M., Giocoli C., Marulli F., Baldi M., 2020, A&A, 634, A135
Gnat O., Sternberg A., 2007, ApJS, 168, 213
Grand R. J. J. et al., 2017, MNRAS, 467, 179
Grand R. J. J., Fragkoudi F., Gómez F. A., Jenkins A., Marinacci F., Pakmor R., Springel V., 2024, MNRAS, 532, 1814
Gutcke T. A., Stinson G. S., Macciò A. V., Wang L., Dutton A. A., 2017, MNRAS, 464, 2796
Gutcke T. A., Pakmor R., Naab T., Springel V., 2021, MNRAS, 501, 5597
Hafen Z. et al., 2020, MNRAS, 494, 3581
Hafen Z. et al., 2024, MNRAS, 528, 39
Hani M. H., Ellison S. L., Sparre M., Grand R. J. J., Pakmor R., Gomez F. A., Springel V., 2019, MNRAS, 488, 135
Harris C. et al., 2020, Nature, 585, 357
Ho S. H., Martin C. L., Schaye J., 2020, ApJ, 904, 76
Hummels C. B., Bryan G. L., Smith B. D., Turk M. J., 2013, MNRAS, 430, 1548
Hummels C. B., Smith B. D., Silvia D. W., 2017, ApJ, 847, 59
Hunter J. D., 2007, Comput. Sci. Eng., 9, 90
Ji S. et al., 2020, MNRAS, 496, 4221
Johnson S. D., Chen H.-W., Mulchaey J. S., 2015, MNRAS, 449, 3263
Johnson S. D., Chen H.-W., Mulchaey J. S., Schaye J., Straka L. A., 2017, ApJ, 850, L10
Kannan R., Vogelsberger M., Marinacci F., McKinnon R., Pakmor R., Springel V., 2019, MNRAS, 485, 117
Karakas A. I., 2010, MNRAS, 403, 1413
Katz H., 2022, MNRAS, 512, 348

Kereš D., Katz N., Weinberg D. H., Davé R., 2005, MNRAS, 363, 2
Lehner N. et al., 2013, ApJ, 770, 138
Machado R. E. G., Tissera P. B., Lima Neto G. B., Sodré L., 2018, A&A, 609, A66
Mathur S., Gupta A., Das S., Krongold Y., Nicastro F., 2021, ApJ, 908, 69
McQuinn M., Werk J. K., 2018, ApJ, 852, 33
Mishra N. et al., 2024, ApJ, 976, 149
Mo H., van den Bosch F. C., White S., 2010, Galaxy Formation and Evolution. Cambridge Univ. Press, Cambridge
Moster B. P., Somerville R. S., Maulbetsch C., van den Bosch F. C., Macciò A. V., Naab T., Oser L., 2010, ApJ, 710, 903
Muratov A. L., Kereš D., Faucher-Giguère C.-A., Hopkins P. F., Quataert E., Murray N., 2015, MNRAS, 454, 2691
Oppenheimer B. D., Davé R., Kereš D., Fardal M., Katz N., Kollmeier J. A., Weinberg D. H., 2010, MNRAS, 406, 2325
Pakmor R., Springel V., Bauer A., Mocz P., Munoz D. J., Ohlmann S. T., Schaal K., Zhu C., 2016, MNRAS, 455, 1134
Peeples M. S., Werk J. K., Tumlinson J., Oppenheimer B. D., Prochaska J. X., Katz N., Weinberg D. H., 2014, ApJ, 786, 54
Planck Collaboration XVI, 2014, A&A, 571, A16
Portinari L., Chiosi C., Bressan A., 1998, A&A, 334, 505
Rahmati A., Pawlik A. H., Raičević M., Schaye J., 2013, MNRAS, 430, 2427
Ranjan A. et al., 2022, A&A, 661, A134
Sales L. V., Wetzel A., Fattahi A., 2022, Nat. Astron., 6, 897
Sanchez N. N., Werk J. K., Tremmel M., Pontzen A., Christensen C., Quinn T., Cruz A., 2019, ApJ, 882, 8
Schaye J. et al., 2015, MNRAS, 446, 521
Springel V., 2010, MNRAS, 401, 791
Springel V., Hernquist L., 2003, MNRAS, 339, 289
Stern J., Fielding D., Faucher-Giguère C.-A., Quataert E., 2019, MNRAS, 488, 2549
Strawn C., Roca-Fàbrega S., Primack J., 2023, MNRAS, 519, 1
Tchernyshyov K. et al., 2022, ApJ, 927, 147
Thielemann F. K. et al., 2003, Nucl. Phys. A, 718, 139
Travaglio C., Hillebrandt W., Reinecke M., Thielemann F. K., 2004, A&A, 425, 1029
Tumlinson J. et al., 2011, Science, 334, 948
Tumlinson J. et al., 2013, ApJ, 777, 59
Tumlinson J., Peeples M. S., Werk J. K., 2017, ARA&A, 55, 389
van de Voort F., Schaye J., 2012, MNRAS, 423, 2991
van de Voort F., Springel V., Mandelker N., van den Bosch F. C., Pakmor R., 2019, MNRAS, 482, L85
Vogelsberger M., Genel S., Sijacki D., Torrey P., Springel V., Hernquist L., 2013, MNRAS, 436, 3031
Wang P., Abel T., 2008, ApJ, 672, 752
Wang L., Dutton A. A., Stinson G. S., Macciò A. V., Penzo C., Kang X., Keller B. W., Wadsley J., 2015, MNRAS, 454, 83
Weng S., Péroux C., Ramesh R., Nelson D., Sadler E. M., Zwaan M., Bollo V., Casavecchia B., 2024, MNRAS, 527, 3494
Werk J. K., Prochaska J. X., Thom C., Tumlinson J., Tripp T. M., O'Meara J. M., Peeples M. S., 2013, ApJS, 204, 17
Werk J. K. et al., 2016, ApJ, 833, 54
Wiersma R. P. C., Schaye J., Smith B. D., 2009, MNRAS, 393, 99
Wright R. J., Lagos C. d. P., Power C., Correa C. A., 2021, MNRAS, 504, 5702
Zheng Y. et al., 2024, ApJ, 960, 55

This paper has been typeset from a TEX/LATEX file prepared by the author.